Observation of the concurrent creation and annihilation of periodic orbits in a nonlinear *RLC* circuit

T. C. Newell,* V. Kovanis,† A. Gavrielides,‡ and P. Bennett
Nonlinear Optics Center, Phillips Laboratory, PL/LIDN 3550 Aberdeen Avenue SE, Kirtland Air Force Base, New Mexico 87117-5776
(Received 23 May 1996)

We have numerically investigated and experimentally demonstrated the presence of antimonotonicity: the concurrent creation and destruction of periodic orbits in a driven nonlinear *RLC* circuit. A simple manifestation of antimonotonicity is the formation of dimples in a high iterate return map. The evolution of such dimples allows for both contact making and contact breaking homoclinic tangencies of the stable and unstable manifolds. Both numerical and experimental return maps unequivocally exhibit the formation of such dimples. The experimental time series were captured using a 16-bit resolution digitizer allowing for a faithful computation of the high iterate return maps. [S1063-651X(96)11610-X]

PACS number(s): 05.45.+b

I. INTRODUCTION

The logistic map has been established as the paradigm for studies of the period doubling route into chaos. Its behavior is *monotone* in the sense that the created orbits are never destroyed through reversals of period doubling cascades. [See Fig. 1(a).] In contrast, a system that can undergo an infinite cascade of orbit creating bifurcations concurrently with an annihilating cascade of reverse bifurcations on continuous variation of a chosen system parameter has been designated *antimonotone* [1]. Antimonotonicity is due to tangential intersections between the stable and unstable manifolds of a system. A one-dimensional cubic map, shown in Fig. 1(b), displays this kind of phenomenon. On comparison with Fig. 1(a), this diagram shows a distinctly chaotic region that was initially born through period doubling and saddle node bifurcations and then subsequently destroyed through the inverse process.

Antimonotonicity has been explored in two-dimensional systems [1,2] and one-dimensional maps [3–5]. For the two-dimensional case, Kan and Yorke have proven antimonotonicity occurs at an existing nondegenerate homoclinic tangency of stable and unstable manifolds. Here the requirement of nondegeneracy specifies that the *velocity* of the two manifolds with respect to the control parameter be nonzero in this region. When the system resides in this type of state, homoclinic tangencies will not only be created, but also destroyed as the parameter is varied. Such events are important for they lead to period doubling and saddle point bifurcations [6]. While the making of a homoclinic tangency can be associated with the creation of orbits, its counterpart incites the destruction of these orbits. Antimonotonocity is the manifestation of these continuously occurring events. While no proof yet exists for the one-dimensional case, Dawson, Grebogi, and Koçak showed that the evolution of a high iterate return map makes and breaks homoclinic tangencies [5]. This mechanism is known as *dimple formation*. In analogy to the two-dimensional story, the formation of dimples signals the concurrent creation and destruction of periodic orbits.

There are a large number of systems that follow an *inverse* period doubling [7] route out of chaos after arriving at that state through the period doubling route. Historically, the first systems showing this effect were driven nonlinear electronic resonators. Here one varied the characteristics of the sinusoidal driving wave such as a dc component [8–10], the frequency of modulation [11], or both the frequency and amplitude of modulation [12]. The Belousov-Zhabotinski chemical reaction also displayed evidence of this behavior when the chemical residence time was utilized as a control parameter [13]. An elegant observation of a forward and inverse cascade of period doublings was recorded using a carbon dioxide laser whose optical cavity length was modulated [14]. Bifurcation diagrams were obtained as a function of the amplitude of modulation. A neodymium doped fiber laser pumped with a laser diode has shown a period doubling cascade along with inverse period doubling [15]. In this experiment, the pump current was modulated sinusoidally. The bifurcation parameter was the frequency of the pump. A semiconductor laser with optical injection displayed evidence of inverse period doubling [16]. In this case, the injection strength serves as the bifurcation parameter. However, because of the fast time scales, measurements for this system are limited to the Fourier domain.

Numerical studies have demonstrated this structure in the Duffing equation [17] and the Van der Pol oscillator [18]. The control parameter in both studies was the frequency of modulation in the driving term. The carbon dioxide laser model used in Ref. [19] exhibits a single forward and inverse period doubling as a function of the detuning between the center of the emission line and laser cavity. A model for an erbium doped fiber laser [20] has also shown inverse period doubling when the concentration of erbium ion pairs in the fiber core increases. A model of magnetoconvection undergoes the forward cascade into an aperiodic state followed by the inverse process as the Rayleigh number is increased [21]. Similarly in maps, the Bier-Bountis maps [22], Hénon map [3], Gaussian map [9], and different versions of the cubic map [4,5,23] possess the property of forward and inverse

*Electronic address: newell@hpruby.plk.af.mil
†Electronic address: kovanis@xaos.plk.af.mil
‡Electronic address: tom@photon.plk.af.mil

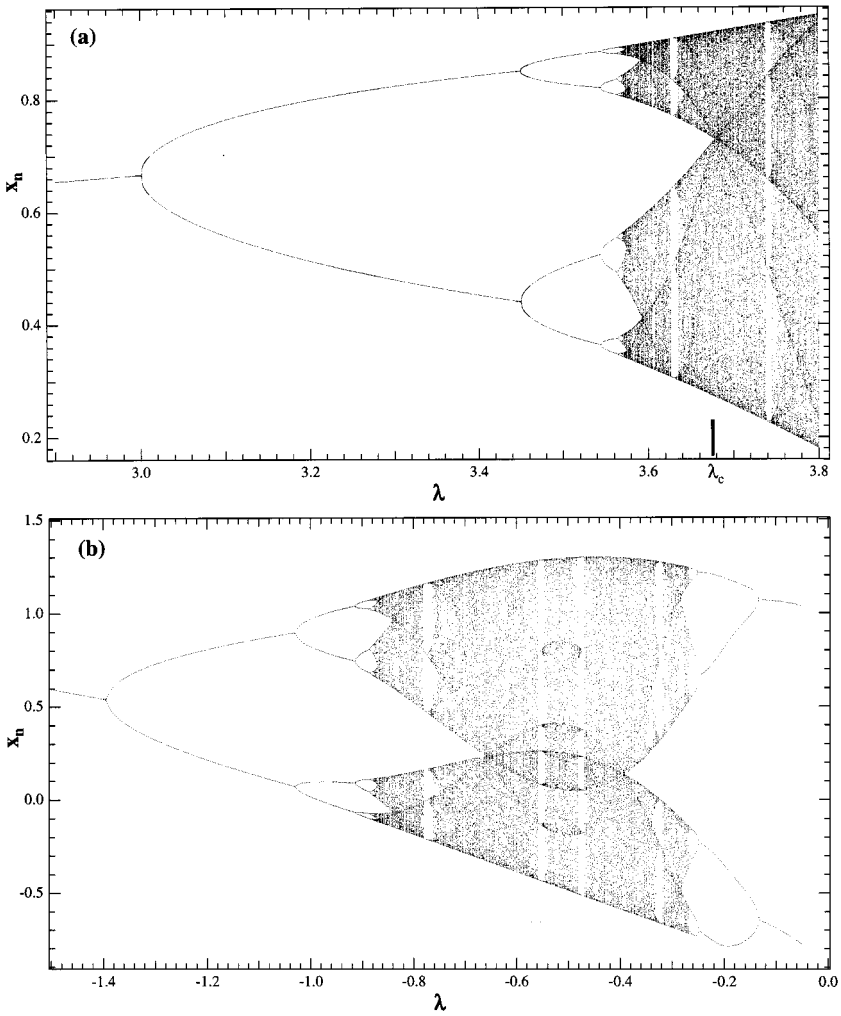

FIG. 1. (a) The monotone creation of orbits is shown in the logistic map. Only period doubling and saddle point bifurcations can be observed. Odd period orbits first begin to appear at the accumulation point $\lambda=\lambda_c\approx 3.679$. (b) The destruction of previously created orbits through inverse period doublings occurs in the map, $x_{n+1}=x_n^3-1.8723x_n-\lambda$ as λ increases.

cascades making them candidates for the presence of antimonotonicity.

In spite of the numerous experimental observations of the concurrent cascades, the mechanism that incites this behavior has yet to be demonstrated. Our motivation in this paper is to investigate this evidence of antimonotonicity. We present numerical studies and experimental results for the case of a driven nonlinear electronic resonator. For this system, a return map generated from successive piercings of a Poincaré section is approximately one dimensional. As a result, we focus on the response of the return map to variations in a system parameter. We show that the making and breaking of homoclinic tangencies as seen in topologically similar one-dimensional maps occurs in the resonator [24]. This establishes that the same mechanism responsible for antimonotonicity in one-dimensional maps also occurs in low-dimensional dynamical systems.

This paper is organized as follows. In Sec. II the geometric mechanism of dimple formation is outlined. Numerical results showing the dimple formation in a driven RLC circuit are presented in Sec. III. In Sec. IV, the experimental setup is described. In Sec. V, the experimental observation of dimples in high iterate maps is presented. These corroborate the numerical results and display similar behavior to the type of one-dimensional maps that exhibit antimonotonicity. Section VI summarizes our main findings. In the Appendix we present details about the RLC circuit model.

II. THE DIMPLE FORMATION MECHANISM IN A ONE-DIMENSIONAL MAP

Curiously, it is more difficult to establish rigorously a conclusion concerning antimonotonocity for a one-dimensional map than it is for a two-dimensional one. The reason is that the one-dimensional map must be noninvertible for chaotic dynamics to occur. However, Dawson, Koçak, and Grebogi [5] have presented a geometric mechanism that demonstrates contact making and contact breaking homoclinic tangencies for scalar maps. This mechanism is a dimple formation that occurs in the structure of a high iterate return map.

We will outline this idea in this section. As a simple yet instructive review of a homoclinic tangency, consider the logistic map,

$$F(x_n)=\lambda x_n(1-x_n), \tag{2.1}$$

at the accumulation point $\lambda=\lambda_c\approx 3.679$. [See Fig. 1(a) at λ_c.] At this interesting point the upper and lower chaotic regions spawned from each branch of the period-2 orbit

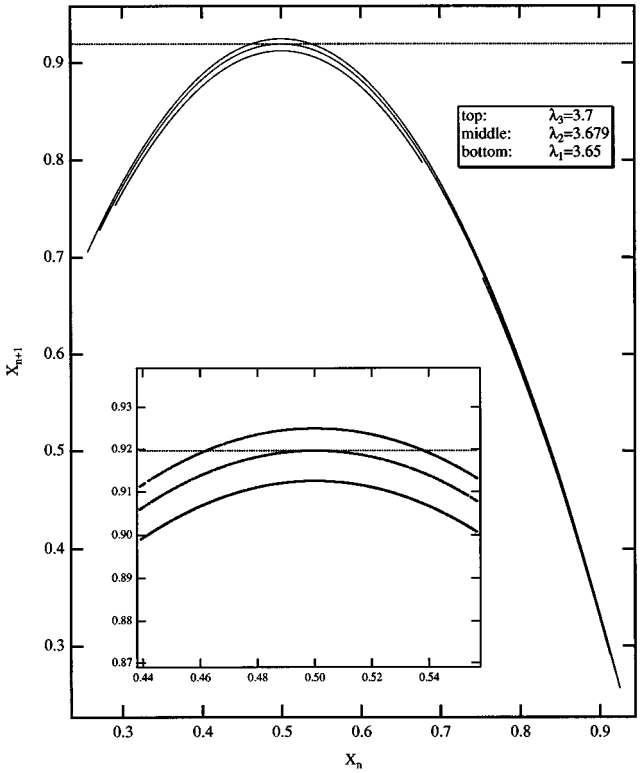

FIG. 2. A contact making homoclinic tangency occurs in the logistic map at $\lambda \approx 3.679$ (middle plot). At this value the critical point maps into the fixed point whose third preimage is indicated by the horizontal line. At $\lambda = 3.65$ (lower plot), the homoclinic tangency has not yet occurred while at $\lambda = 3.7$ (upper plot) two transverse homoclinic points exist. The inset is an enlargement of the region around the critical point.

merge. Here according to Sharkovski's ordering [25], all orbits whose period is a power of 2 have been created and the odd periods begin to appear.

The logistic map computed for three values of λ that are below, equal, and above λ_c is shown in Fig. 2. The inset is a close-up of the region around the critical point, $c_1 = 0.5$ $[dF(x_n)/dx_n = 0, x_n = c_1, c_2]$. The horizontal line indicates the second preimage, $x_2 \approx 0.920$, to the fixed point, p, when $\lambda = \lambda_c$,

$$F^{-2}(p, \lambda_c) = x_2 . \tag{2.2}$$

Note that since here $p = (\lambda - 1)/\lambda$, increasing λ causes an upward movement in p and a corresponding shift in x_2. However, this displacement is relatively small compared to the shift in the map. For the map computed at $\lambda < \lambda_c$, there is no contact between the preimage to p and the map. When $\lambda = \lambda_c$, the map makes tangential contact at c_1 with the preimage line. At this point, a homoclinic tangency has occurred since $F^2(c_1, \lambda_c) = p$. An infinite number of orbits follows from this contact. For $\lambda > \lambda_c$, two transverse homoclinic points exist. Now the limitation of unimodal maps is that only contact making homoclinic tangencies occur. The single critical point constrains the motion of the map and its forward iterates to always evolve similarly to that seen in Fig. 2. Correspondingly orbits are only created.

How then does antimonotonicity occur in a one-dimensional map? Dawson *et al.* [4,5] postulated and numerically substantiated that the occurrence of two critical points simultaneously residing in a chaotic attractor are, in general, sufficient for antimonotonicity. The two critical points allow contact breaking homoclinic tangencies that reverse the process of the contact making homoclinic tangencies. Consider the one-dimensional scalar map,

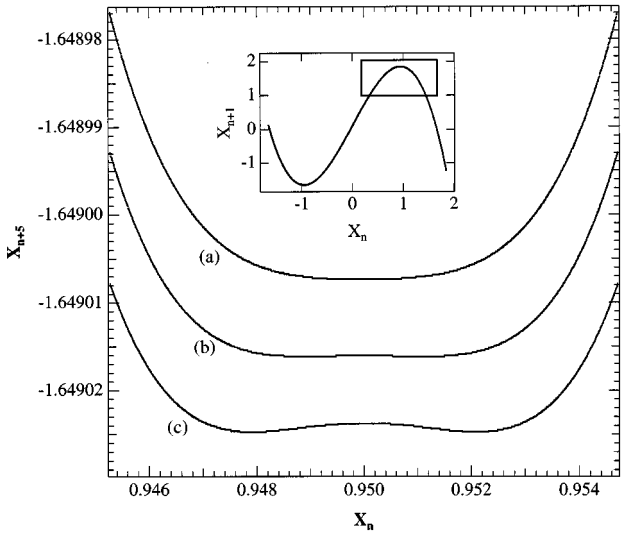

FIG. 3. A dimple forms in the fifth forward iterate of the map, $x_{n+1} = \alpha x_n (3c^2 - x_n^2) + 0.099$ $(c = 0.95)$ [5]. Plotted is the map for $\alpha = 1.019\,395$ (a), $\alpha = 1.0194$ (b), and $\alpha = 1.019\,405$ (c). These local extrema make and break tangential contact with preimages of the fixed point. This process generates concurrent creation and destruction of periodic orbits.

$$F(x_n, \lambda) = \lambda x_n (3c^2 - x_n^2) + 0.099, \tag{2.3}$$

where $c = 0.95$, and the critical points are $c_1 = 0.95$ and $c_2 = -0.95$ [5]. A bifurcation diagram of this map is shown in Fig. 1(b). The map itself is displayed in the inset of Fig. 3. We want to observe the mapping of the critical point, c_1, and the evolution of the neighborhood surrounding this point as we vary λ. We can expect that here, and in general, after some number of iterates one critical point, c_1, will map into the other, c_2, i.e., $F^j(c_1, \lambda_c) = c_2$. That iterate is 4 when $\lambda = \lambda_c \approx 1.019\,398$, $F^4(c_1, \lambda_c) = c_2$. Furthermore, after some additional number of iterations, c_1 will map into the vicinity of the fixed point. Both statements are due to the ergodic nature of trajectories in a chaotic attractor. Analogously to the logistic map, homoclinic tangencies will occur for this map as it evolves.

The stage is now in place for the formation of dimples. We investigate the $(j+1)$st forward return map (here $j = 4$) in the neighborhood of the critical point c_1. Figure 3 shows the fifth forward iterate of the map around c_1, for three values of λ. At this iterate a quartic critical point exists at c_1 and $\lambda = \lambda_c$. This can be understood by considering the derivative of F^{j+1} with respect to x at $x = c_1$. As λ is increased above λ_c, c_1 no longer maps directly into c_2. The point dimples inwards creating three extrema from the one extremum. In Fig. 3 for $\lambda = 1.019\,395$ [the upper curve marked (a)], the map has a parabolic type shape. For $\lambda = 1.0194$ [the middle curve marked (b)] and $\lambda = 1.019\,405$ [the lower curve, marked (c)], the critical point

inflects upwards clearly forming a dimple. There are an infinite number of preimages to the fixed point between the middle and lower curves of Fig. 3. As the map evolves, the outer two extrema make homoclinic tangencies with these preimages. However, the inner extremum breaks contact with these preimages. Antimonotonicity is the result of this display of contact making and contact breaking homoclinic tangencies.

III. NUMERICAL INVESTIGATIONS OF DIMPLE FORMATION IN THE *RLC* CIRCUIT

A large class of physical systems can be described by one-dimensional maps. Consequently, the observation of the dimple formation mechanism in these particular maps is an important step in providing evidence for the existence of antimonotonicity. In this section we concentrate our effort on a nonlinear electronic resonator. Specifically, our aim is to generate a map from a numerical model of the resonator and observe whether this map displays the dimple formation mechanism as described above.

This resonator is a sinusoidally driven electrical circuit composed of a $p-n$ junction diode in series with an inductor and a resistor [26,27]. A third order ordinary differential equation model is derived by considering the diode as a nonlinear capacitor in parallel with a nonlinear resistor [28]. The dimensionless equations of the model are

$$\dot{I}(\tau)=V_0\sin(\tau)-V(\tau)-\beta I(\tau)+V_d, \tag{3.1}$$

$$\dot{V}(\tau)=G(I,V), \tag{3.2}$$

$$\dot{\tau}=2\pi f. \tag{3.3}$$

The pertinent terms are I, the current through the resistor, V, the voltage drop across the diode, and V_d, a bias voltage that serves as the bifurcation parameter. The other terms are defined in the Appendix.

A computed bifurcation diagram of the current peaks taken as V_d is added to the driving wave is presented in Fig. 4. Here $f=70$ kHz and $V_0=2.8$ (dimensionless). The diagram displays three bands of chaotic regions. Originally in a period-1 orbit, the resonator period doubles into a chaotic regime at $V_d=-2.62$, then inverse period doubles to a period-2 orbit at $V_d=-2.0$ V. Between $V_d=-2.62$ and $V_d=-2.0$, the resonator has inverse period doubled out of chaos to a period-4 orbit at $V_d=-2.36$, then back into and out of other regimes.

The resonator undergoes a period doubling cascade back into chaos once V_d increases above -2.0 V. This is followed by a saddle node bifurcation into a period-3 orbit. Ordinarily one would expect the system to bifurcate into period-6 and beyond. However, here an apparent reversal of a tangent bifurcation trips the resonator back into a chaotic regime. It finally returns to a period-1 orbit through reverse bifurcations.

The dominant region of interest is the first band of chaotic behavior. This is shown in Fig. 4(b). A myriad of forward and inverse period doublings along with various periodic windows are shown in this figure. Between $V_d=-2.64$ and -2.48 a chaotic band exists which was entered through a period doubling cascade and exited through the inverse process. While this diagram is visually indicative of antimonotonicity, we investigate this particular region in order to substantiate the evidence.

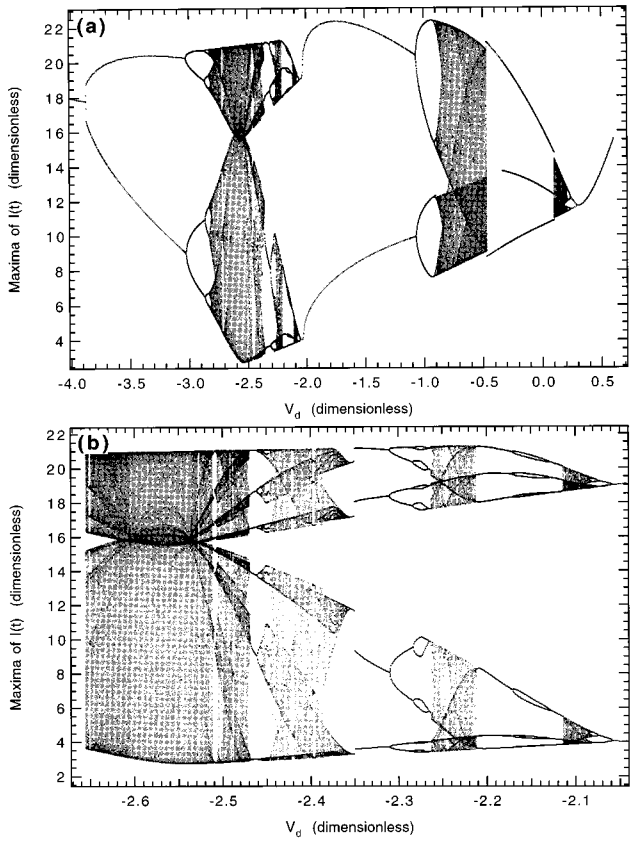

FIG. 4. (a) A prolific display of bifurcation processes is manifested in this numerical bifurcation diagram of the nonlinear electronic resonator. The maxima of the resonator current are plotted versus an applied bias voltage. (b) The first chaotic regime in (a) is expanded. This chaotic region is a candidate for the observance of both contact making and breaking homoclinic tangencies.

We desire to determine if contact making and contact breaking homoclinic tangencies are occurring. In order to do so, return maps are extracted for various values of V_d. The evolution of these maps is studied analogously to the cubic map above. Figure 5 is a first return map of the current peaks [the maxima of I versus $I(n+1)$], taken for $V_d=-2.6$. It is reminiscent of the logistic map except for the folded inward section on the right-hand side. Hence the map has two critical points. On closer inspection there is a degree of structure indicative of a higher dimensional system. A calculation of the Lyapunov exponents gives a spectrum of $\lambda_1=0.055$, $\lambda_2=0$, and $\lambda_3=-0.234$ [29]. From these, the Kaplan-Yorke dimension is 1.24.

Marked on Fig. 5 are points c_1 through X_5 that show the forward iterates of c_1. This point is immediately mapped into the second critical point, c_2. After two more iterates c_1 maps to X_5 which is quite near the unstable fixed point of the map, p. We therefore expect that for some value of offset, a homoclinic tangency will occur as c_1 is mapped into p. According to the discussion concerning the cubic map, a dimple process should begin on the second iterate return map at the appropriate value of V_d. This dimple formation will also be displayed in higher iterate return maps. Therefore, we will

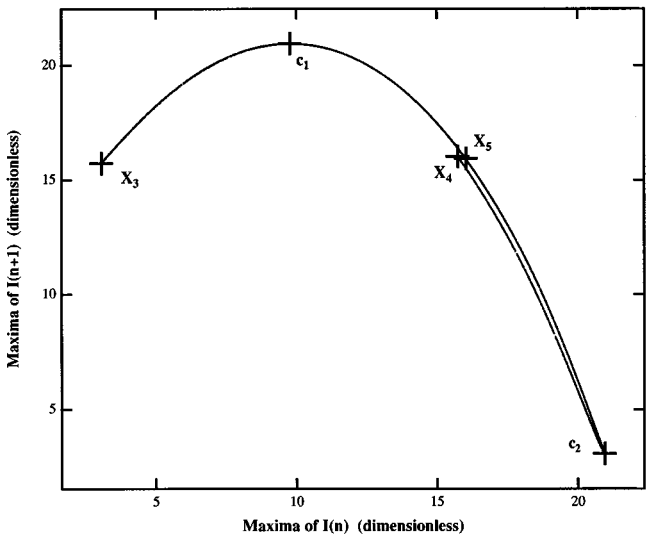

FIG. 5. The computed first return map of the resonator is reminiscent of the logistic map but folds inward in the upper region. The central critical point, marked as c_1, maps on the next iterate to the upper critical point, c_2. Three iterates later, the mapping takes us to X_5, which is in the vicinity of the fixed point, p. As V_d is varied, X_1 will map to p creating a homoclinic tangency.

look at the evolution of the second return map experimentally below and will study numerically how the critical point is mapped into the vicinity of p in a fifth return map here.

A fifth return map with $V_d=-2.6$ is shown in its entirety in Fig. 6(a). In the vicinity of the critical point (marked by the box), the map has a parabolic type curve. Figure 6(b) is a close-up of the boxed area in Fig. 6(a). In addition to the map at $V_d=-2.60$ (the central set of points), maps at $V_d=-2.62$ (the upper set of points) and $V_d=-2.58$ (the lower set of points) are also plotted. The horizontal line in the graph indicates the position of the fixed point. At $V_d=-2.62$, c_1 does not yet map into the fixed point. However, a contact making homoclinic tangency is about to occur when $V_d=-2.60$. Finally at $V_d=-2.58$ the critical point maps beyond the fixed point and transversal homoclinic points exist on both sides of c_1. The bifurcation diagram, Fig. 4, shows the creation of orbits as the system moves into a region of fully developed chaos.

Bifurcations out of chaos can be seen further along Fig. 4. A fifth return map for $V_d=-2.54$ is shown in Fig. 7(a). While it has the same general look as Fig. 6(a), note that the boxed region around the critical point is dimpled inwards. This area is enlarged in Fig. 7(b). Again three maps are plotted, but now as the offset is increased, the maps dimple and recede upwards. For $V_d=-2.550$ points straddling the critical point make contact with the fixed point. The map retreats upwards as the critical point inflects upwards. At $V_d=-2.532$ the homoclinic tangency is breaking. Finally when $V_d=-2.526$ there is no local contact. Figure 4 shows the destruction of orbits as the resonator period halves towards the period-4 orbit.

IV. EXPERIMENTAL SETUP

Our experimental setup shown in Fig. 8 is composed of a 1N4004 silicon rectifier diode, a 47 mH inductor with an

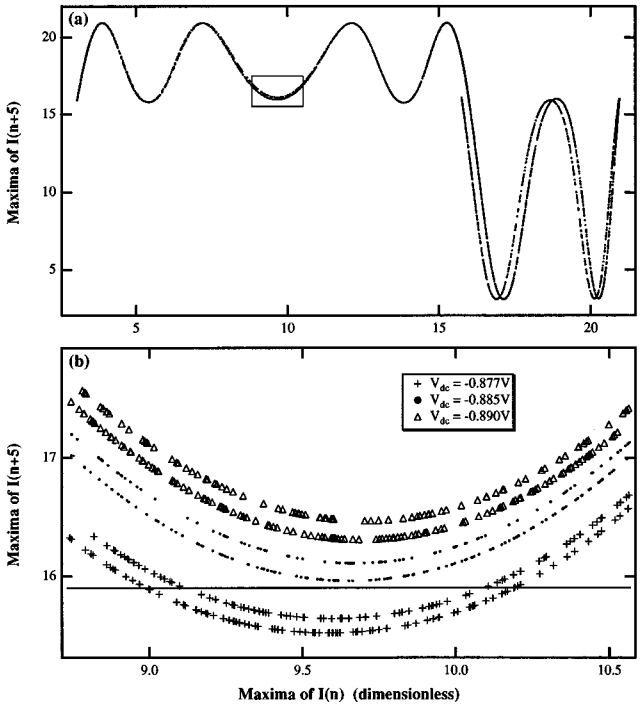

FIG. 6. (a) The numerical fifth return map of the maxima of $I(n)$ versus $I(n+5)$ when $V_d=-0.885$ V. The boxed area focuses attention on the critical point. An enlargement of the boxed area is shown in (b). In addition to $V_d=-2.604$ V, maps are plotted for $V_d=-0.89$ V and $V_d=-0.877$ V. The three maps show the making of a homoclinic tangency.

internal resistance of 368Ω, and a 330Ω resistor in series with the other two components. The resonator is dc biased and sinusoidally driven, $V_d+V_0\sin 2\pi ft$, by a Hewlett-Packard programmable function generator (HP3325*A*). A LH0002 line driver buffers the function generator from the resonator and provides a spectrally pure sinusoidal drive wave. The voltage drop across the resistor, $V(t)$, is amplified by a low noise Stanford Research Systems SRS560 preamplifier then digitized with a 16-bit resolution 1 megasample per second Analogic FAST16 digitizer. A personal computer coordinates the equipment and acquires the incoming data. Finally, we thermally stabilize the resonator at $3°\pm0.05°$C in a dewar flask. This minimizes the influence of the ambient temperature on the bifurcation points of the resonator.

We probe the dynamics of the resonator by setting V_0 and then stepping V_d while recording time series at each 1 mV increment. The driving frequency, f, is always kept constant at 40 kHz. Long 16-bit resolution time series of $V(t)$ are acquired, and points in the vicinity of the maxima are extracted. A cubic polynomial curve fit scaled to the digitizer resolution is performed to approximate the true maxima. As a last step in data processing, we histogram the peaks in bins based on the resolution of the digitizer. This provides a statistical look at the relative density of peaks. Plots of the resulting bifurcations, $V_r(t_{\text{peak}})$ vs V_{dc}, are then grey scale coded to represent the density of occurrence. In spite of this effort, the inevitable noise in the entire arrangement coupled with the consequences of the universal scaling law for period doubling bifurcations tends to harness the possibility of di-

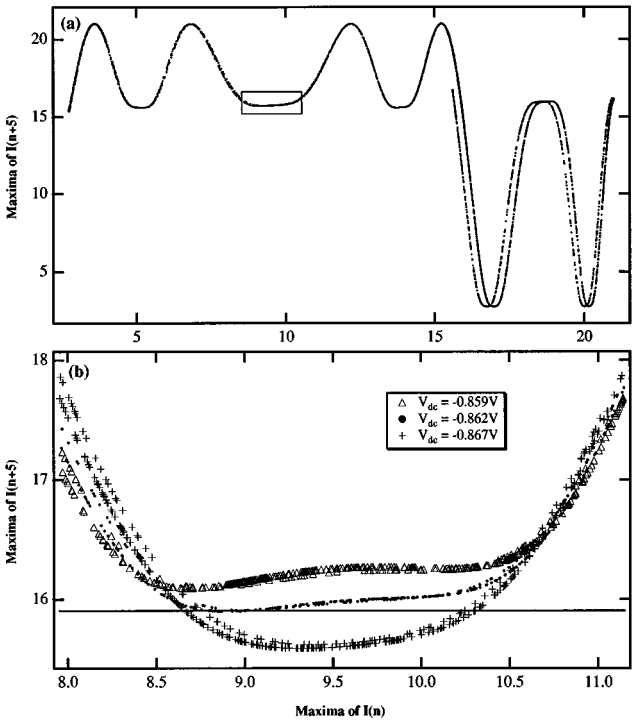

FIG. 7. (a) The fifth return map of the maxima of $I(n)$ versus $I(n+5)$ computed for $V_d=-0.862$ V. (b) An enlargement of the boxed area. In addition to $V_d=-2.534$ V, maps are plotted for $V_d=-0.867$ V and $V_d=-0.859$ V. These maps indicate the breaking of a homoclinic tangency. The extrema of the dimple make and break contact with the infinite number of preimages to the fixed point. The result is antimonotonicity.

rect observation of high period orbits [30].

V. OBSERVING THE FORMATION OF DIMPLES

Bifurcation diagrams of the maxima of $V(t)$ versus V_d for four values of V_0 are shown in Fig. 9. In all cases, when V_d is low, the diode is predominantly reverse biased and

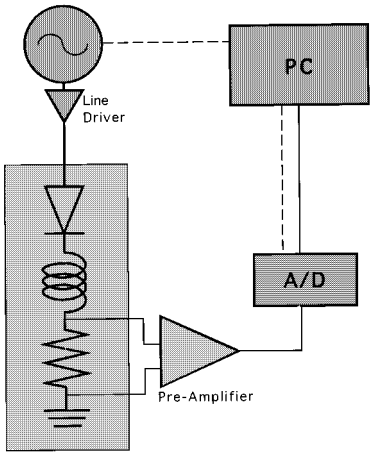

FIG. 8. The experimental setup is organized around the sinusoidally driven RLC circuit. Data are acquired with a 16-bit resolution 1 megasample/sec digitizer and stored in the computer. The sine wave generator and digitizer are controlled by the computer.

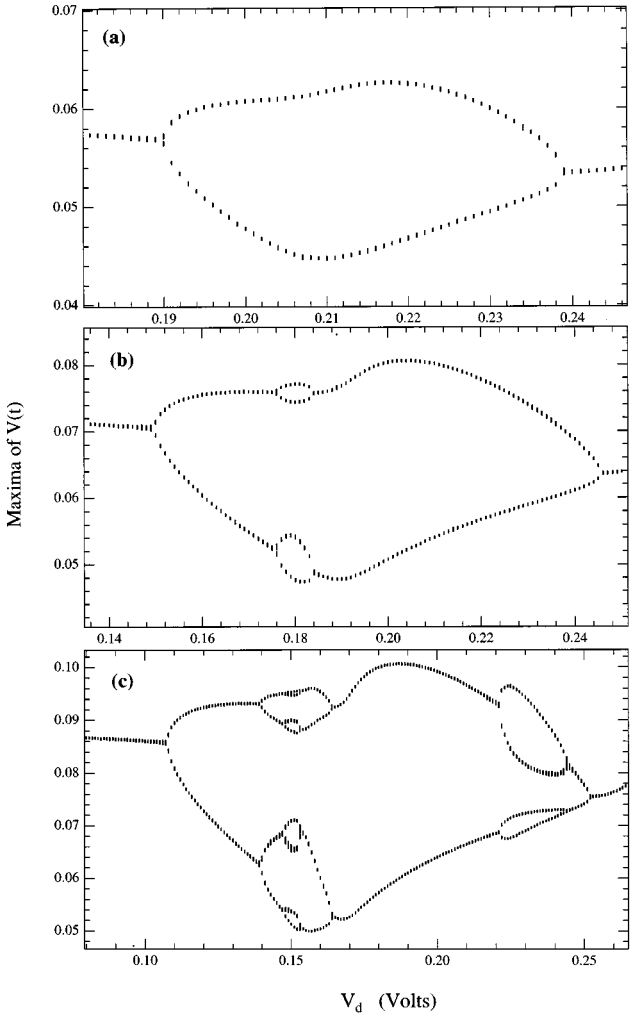

FIG. 9. Experimental bifurcation diagrams for different levels of drive amplitude. (a) At $V_0=0.3$ V a period-2 bubble forms. Below this value, the resonator never bifurcates. (b) At $V_0=0.5$ V the $f/2$ bifurcation point has shifted downwards and a period-4 orbit appears. (c) Two regions of bubbling have appeared as well as a period-8 orbit by the time $V_0=0.75$ V.

essentially acts as a high impedance device. At the other end of the scale, the diode is mostly forward biased and tends to act as a linear element. This explains the period-1 orbit for both low and high values of dc offset. In the intermediate regions depending on the value of V_0, the motion of the charge carriers in the diode creates the rich dynamical features. At very low drive amplitudes V oscillates in a period-1 orbit regardless of the dc offset, V_d.

At $V_0=0.3$ V [Fig. 9(a)], a period doubling bifurcation occurs when $V_d=0.189$ V. A strong $f/2$ frequency component appears in the Fourier spectrum. The system remains in this state until $V_d=0.239$ V, at which point an inverse period doubling occurs. The resonator returns to the period-1 orbit and the $f/2$ frequency component attenuates almost completely. We refer to this as an $f/2$ *bubble* [22,9].

When $V_0=0.5$ V [Fig. 9(b)], after the $f/2$ period doubling, a second period doubling creates an $f/4$ bubble at $V_d=0.17$ V. As we increase V_d, two inverse period doublings return the resonator to its period-1 state. At $V_0=0.75$ V, Fig. 9(c), the cascade continues with the appear-

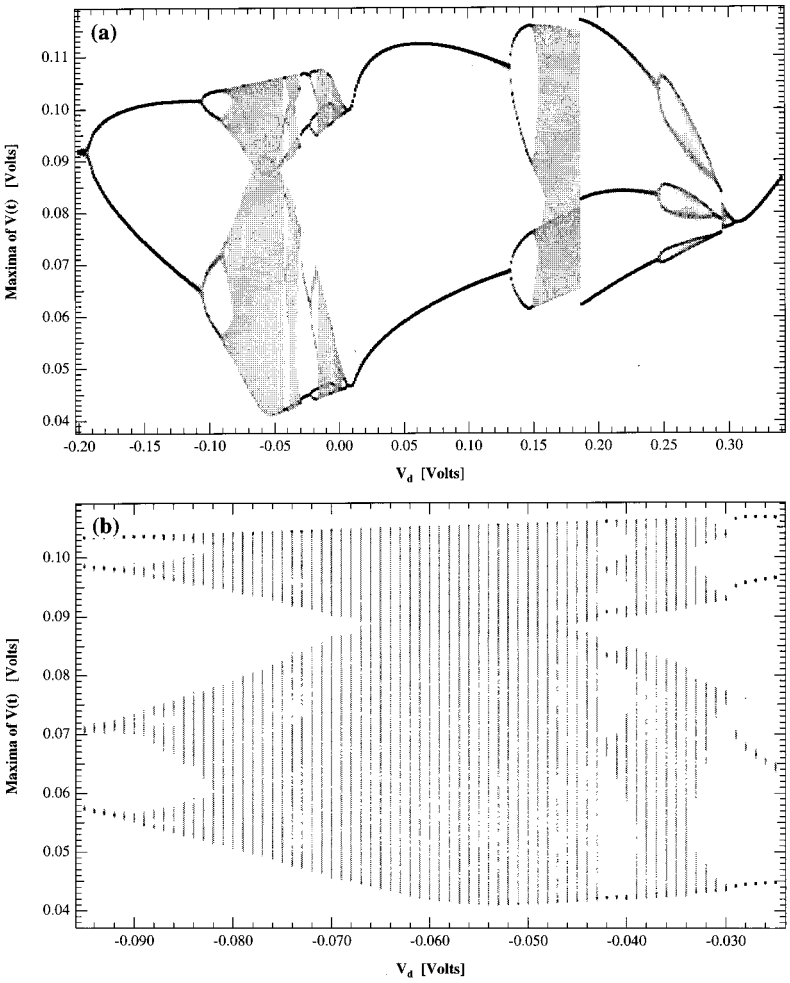

FIG. 10. (a) A bifurcation diagram when $V_0=3$ V. Chaotic bands have emerged as a result of the bubbling cascade. (b) A zoomed region of the first chaotic band indicates that created orbits are destroyed as the resonator moves into a $f/4$ cycle. This region is a candidate for the observation of homoclinic tangencies.

ance of an $f/8$ bubble at $V_d=0.16$ V. We also find that another $f/4$ bubble appears at $V_d=0.23$ V. Bifurcation diagrams taken for increasing values of the drive amplitude would show a series of forward and inverse bifurcations occurring in bands until chaotic states are reached. These periodic bubbles are not limited to the resonator. They can also be observed in maps [23,22,31,9] and fiber lasers [32].

Figure 10(a) displays the accumulation of bubbling that has led to the chaotic bands. It is quite similar to Fig. 4 except for three bubbles that have formed between $V_d=0.25$ V and $V_d=0.3$ V. As in the previous bifurcation diagrams, the resonator commences with a limit cycle oscillating at f, then undergoes a visible $f/2$, $f/4$, and $f/8$ period doubling at $V_d=-0.195$V, -0.106 V, and -0.090 V, respectively. The resonator enters a chaotic region that includes forward and reverse pitchforks. This particular region between $V_d=-0.09$ V and -0.04 V is shown in Fig. 10. The resonator period doubles into chaos and then appears to inverse period double above $V_d=-0.050$ V. It subsequently undergoes a tangent bifurcation at $V_d=-0.042$ V and then undergoes a series of period doublings followed by inverse period doublings into a period-4 orbit above $V_d=-0.031$ V. As V_d increases above 0.0 V, the system inverse period doubles back into an $f/2$ region. Another period doubling cascade commences when $V_d=0.132$ V. This cascade continues into a chaotic regime. At $V_d=0.186$ V, a tangent bifurcation [7] occurs latching the resonator into an $f/3$ region. An $f/6$ orbit is subsequently born at $V_d=0.245$ V. Forward followed by inverse period doubling bifurcations occur at higher values of V_d. Then at $V_d=0.295$ V, an inverse tangent bifurcation brings the resonator into a chaotic zone. It then inverse period doubles into the limit cycle at $V_d=0.305$ V.

The first chaotic region is expanded in Fig. 10(b). The structure of the bifurcation diagram indicates that making and breaking of homoclinic tangencies may be occurring. We wish to investigate this region and experimentally ascertain if a dimple formation mechanism is responsible. Figure 11(a) shows a first return map taken at $V_d=-0.06$ V. It is very similar to the numerically computed map, Fig. 5. The central critical point, c_1, maps directly into the second critical point. In accordance with the dimple formation mechanism, a quartic critical point at c_1 will occur for the second iterate return map, maxima of $V(n)$ vs maxima of $V(n+2)$. Consequently we expect to see the beginning of dimpling in a second return map.

Figure 11(b) is an experimental second return map taken when $V_d=-0.057$ V. Focus on the boxed region. Figure 11(c) shows a close up of the region of points surrounding c_1 for $V_d=-0.064$ V, -0.061 V, and -0.055 V. The horizontal line designates the location of the second preimage of the fixed point. As V_d is increased, the map pushes

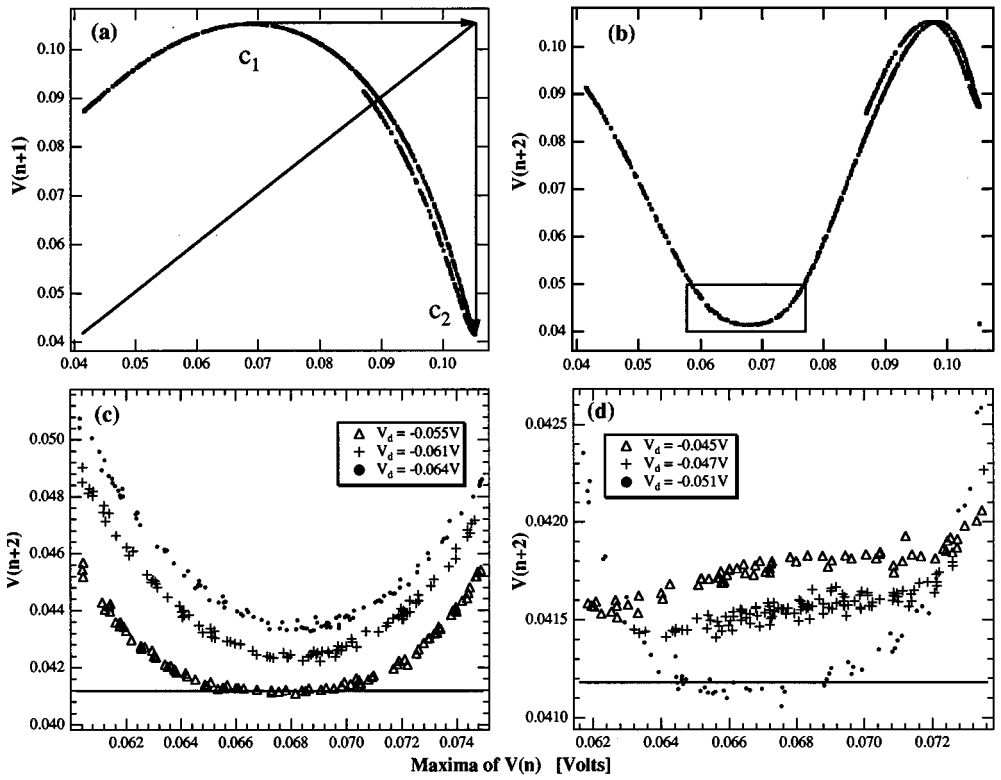

FIG. 11. First (a) and second (b) return maps of the maxima of $V(t)$. (a) This map is indicative of one-dimensional maps with two critical points: an essential requirement for dimple formation. In the second return map, (b), the neighborhood of points surrounding the critical point (boxed region) is studied in (c) and (d) for dimple formation. (c) As V_d is increased from -0.064 V to -0.055 V the map pushes downwards to the second preimage of the fixed point (the horizontal line). Initial contact with this line shows a contact making homoclinic tangency. (d) As V_d continues to increase the map dimples upwards and inflects inwards breaking an established homoclinic orbit.

downwards towards this point until it roughly makes contact at $V_d=-0.055$ V. This is a strong indication of the contact making homoclinic tangency. Correspondingly, the bifurcation diagram, Fig. 10, displays a region of orbit creation.

We increment V_d and again extract return maps. These are quite similar to Fig. 11(a) and (b) except in the boxed region. This area is enlarged in Fig. 11(d). Maps at $V_d=-0.051$ V, -0.047 V, and -0.045 V are displayed. Here the map begins to recede upwards and inflects inwards. At $V_d=-0.051$ V points straddling c_1 make contact with the preimage. But when $V_d=-0.047$ V followed by $V_d=-0.045$ V the map no longer makes contact with this preimage. This indicates the contact breaking homoclinic tangency. In this region, the bifurcation diagram shows the destruction of orbits as the resonator reverse bifurcates towards a period-4 orbit.

On comparison of this dimpling process with that of the cubic map, Fig. 3, we find that the process is not truly identical. This arises because of the simple nature of the bifurcation parameter, λ, in the cubic map. For the resonator, the role of the bias voltage is more sublime. The return map slightly rotates as V_d increases and it causes an asymmetry in the dimple. Nevertheless, it is clear that the return map of the resonator will make and break contact tangentially with preimages to the fixed point of the map. These figures show solid evidence of the existence of antimonotonicity in the RLC circuit.

VI. SUMMARY

The substantial number of physical systems that exhibit both forward and inverse period doubling cascades motivated our study of antimonotonicity. We were specifically interested in observing the mechanism that incites antimonotone behavior. Our investigation focused on a driven nonlinear RLC electrical circuit. This particular system has a long history of study. Though it is experimentally simple to construct, it displays practically all the processes one normally associates with the study of nonlinear dynamics and chaos.

Numerically, we computed bifurcation diagrams as a function of an added bias voltage, V_d (see Fig. 4). These are in strong qualitative agreement with experimental results, Fig. 9, across a large parameter space. They display a complex bubbling process, including forward and reverse pitchforks. First return maps, extracted from one particular chaotic regime in the bifurcation diagram, are similar to the logistic map but possess two critical points. This is a consequence of the damped nature of the resonator, which produces an approximately one-dimensional attractor. As the return map evolves across the chaotic band, the motion of its critical points make tangential contact with preimages of the fixed point establishing a homoclinic tangency. We next studied a fifth return map in order to observe the evolution of the critical point in the vicinity of the fixed point. As we increase V_d, the critical point dimples inward and the map in this vicinity reverses its direction of motion. The dimpling

process leads not only to contact making homoclinic tangencies but also to contact breaking homoclinic tangencies. This is because the local extrema make and break contact with preimages of the fixed point. This concurrent process is the hallmark of antimonotonicity.

Experimentally an electrical circuit possesses a number of advantages over an optical or chemical system. One has much greater control over many of the parameters which influence the behavior. In particular, by controlling the temperature, we were able to place our *RLC* circuit in a regime that was less noisy and high periodic orbits were more easily captured. We were then able to generate bifurcation diagrams and return maps. These diagrams are highly dependent on the amplitude of the drive signal. For small amplitudes, the resonator will always reside in a period one orbit. When the drive amplitude is larger, bubbles of periodic orbits occur in the bifurcation diagram. As the amplitude is increased, these bubbles expand into bands of chaotic regions indicative of antimonotone behavior. For the last case, second return maps displayed the formation of dimples as V_d increased.

The result of our investigation is evidence that homoclinic tangencies are made and broken through a dimple formation process analogously to the process that occurs in a one-dimensional map that possesses two critical points residing in its chaotic attractor. Since a number of physical systems can be modeled by such maps, a dimple formation process is likely to occur there as well.

ACKNOWLEDGMENTS

The authors would like to thank Celso Grebogi and Ying-Chen Lai for encouragement through the course of this work and helpful discussions. Also we wish to thank R. Kalmus and R. Marquez for technical assistance. Additionally T.C.N. would like to thank the National Research Council for supporting this work.

APPENDIX

The model of the resonator follows from considering the diode as a nonlinear resistor and capacitor and then applying Kirchoff's laws to the circuit [28]. Its nonlinear resistance follows from the familiar *I*-*V* curve found in rudimentary electronics texts. The nonlinear capacitive properties follow from considering the effect an ac signal would have on the transport carriers in the semiconductor material and their recombination around the *p*-*n* junction. The result is that chaotic behavior arises when the carrier transport times are relatively long. Such is the case for this particular family (1N400X) of rectifier diodes. In contrast, fast switching diodes do not appear to display chaotic behavior in this circuit.

TABLE I. Parameter values.

n	1.7	m	0.38
β	0.0215	α	7.69
b_1	0.384	γ	0.275
b_2	0.31	c_1	5.16
c_2	0.078		

The dynamical equations in dimensionless units are shown below. They are expressed in terms of a current, I, and a voltage drop across the diode, V.

$$\frac{dI}{d\tau} = V_0 \sin(\tau) - V - \beta I + V_d , \tag{A1}$$

$$\frac{dV}{d\tau} = G(I,V), \tag{A2}$$

where

$$G(I,V) = \frac{I - \gamma(e^{\alpha V} - 1)}{c_1[e^{\alpha V} + c_2(1-V)^{-m}]} \quad \text{if } V < \frac{1}{2}, \tag{A3}$$

$$G(I,V) = \frac{I - \gamma(e^{\alpha V} - 1)}{c_1\left[e^{\alpha V} + c_2 \dfrac{(b_2 + mV)}{b_1}\right]} \quad \text{if } V \geqslant \frac{1}{2}, \tag{A4}$$

and finally

$$\frac{d\tau}{dt} = 2\pi f. \tag{A5}$$

The drive amplitude V_0, frequency f, and dc offset V_d define the pertinent parameter space. The other parameters relate to the characteristics of a 1N4004 diode and its operating temperature. Experimentally, we find that the properties of diodes vary widely not only from one to another but also from one day to the next. As a result, the parameter values found in Table I are generic for the 1N4004 diode.

For our numerical investigation, we used a fourth order Runge-Kutta integrator. The integration step size for this work was set at 3000 steps/cycle. The bifurcation starts at a dc offset that places the resonator in a periodic orbit. For the first value of V_d, the initial conditions are arbitrary and 2000 time units are integrated to find the attractor before peaks are recorded. Subsequently the final integration result for the nth offset is used as the initial conditions of the $(n+1)$st value. Then only 500 time units are integrated to find the attractor. This is for speed and also assumes that the dc offset increment of 0.001 is small enough so that the initial conditions of the integration are always very close to the attractor. Peaks of the current through the resonator are extracted from a computed time series and used to create the return maps and bifurcation diagrams.

[1] I. Kan and J. Yorke, Bull. Am. Math. Soc. **23**, 469 (1990).
[2] I. Kan, H. Koçak, and J. A. Yorke, Ann. Math. **136**, 219 (1992).
[3] S. P. Dawson and C. Grebogi, Chaos Solitons Fractals **1**, 137 (1991).
[4] S. P. Dawson, C. Grebogi, J. A. Yorke, I. Kan, and H. Koçak, Phys. Lett. A **162**, 249 (1992).
[5] S. P. Dawson, C. Grebogi, and H. Koçak, Phys. Rev. E **48**,1676 (1993).
[6] R. Devaney, *An Introduction to Chaotic Dynamical Systems*

(Benjamin/Cummings, Menlo Park, CA, 1986), p. 121.
[7] E. Ott, *Chaos in Dynamical Systems* (Cambridge University Press, Cambridge, 1993).
[8] J. Cascais, R. Dilao, and A. Noronha Da Costa, Phys. Lett. **93A**, 213 (1983).
[9] R. C. Hilborn, *Chaos and Nonlinear Dynamics* (Oxford University Press, New York, 1994), p. 17.
[10] T. C. Newell, V. Kovanis, and A. Gavrielides, Phys. Rev. Lett. **77**, 1747 (1996).
[11] R. V. Buskirk and C. Jeffries, Phys. Rev. A **31**, 3332 (1985).
[12] M. F. Bocko, D. H. Douglas, and H. H. Frutchy, Phys. Lett. **104**, 388 (1984).
[13] K. Coffman, W. D. McCormick, and H. L. Swinney, Phys. Rev. Lett. **56**, 999 (1986).
[14] T. Midavaine, D. Dangoisse, and P. Glorieux, Phys. Rev. Lett. **55**, 1989 (1985).
[15] D. Derozier, S. Biewlawski, and P. Glorieux, Opt. Commun. **83**, 97 (1991).
[16] T. B. Simpson, J. M. Liu, A. Gavrielides, V. Kovanis, and P. M. Alsing, Phys. Rev. A **51**, 4181 (1995).
[17] U. Parlitz and W. Lauterborn, Phys. Lett. **107A**, 351 (1985).
[18] U. Parlitz and W. Lauterborn, Phys. Rev. A **36**, 1428 (1987).
[19] D. Dangoisse, P. Glorieux, and D. Hennequin, Phys. Rev. A **36**, 4775 (1987).
[20] F. Sanchez and G. Stephan, Phys. Rev. E **53**, 2110 (1996).
[21] E. Knobloch and N. O. Weiss, Physica **9D**, 379 (1983).
[22] M. Bier and T. C. Bountis, Phys. Lett. **104A**, 239 (1984).
[23] G. L. Oppo and A. Politi, Phys. Rev. A **30**, 435 (1984).
[24] G. B. Mindlin *et al.*, Phys. Rev. Lett. **64**, 2350 (1990).
[25] A. N. Sharkovsky, Ukranian Math. J. **16**, 61 (1964).
[26] P. S. Linsay, Phys. Rev. Lett. **47**, 1349 (1981).
[27] J. Testa, J. Perez, and C. Jeffries, Phys. Rev. Lett. **48**, 714 (1982).
[28] See T. C. Newell, P. M. Alsing, A. Gavrielides, and V. Kovanis, Phys. Rev. E **51**, 2963 (1995).
[29] The Lyapunov exponents were computed from H. E. Nusse and J. A. Yorke, *Dynamics: Numerical Exploration* (Springer-Verlag, New York, 1994).
[30] P. Cvitanović, *Universality and Chaos* (Adam Hilger, New York, 1989).
[31] If the cubic map displayed in Fig. 1(b) is computed with values less than 1.8723, the bifurcation diagram will resemble Figs. 9(a)–9(c).
[32] Our experimental investigations of a Nd fiber laser have shown an $f/2$ bubble for certain operating regimes. T. C. Newell *et al.*, OSA Tech. Dig. Ser. **11**, 52 (1996).